Near-Infrared Chiral Plasmonic Microwires Through Precision Assembly of Gold Nanorods on Soft Biotemplates

Amrita Chakraborty,[1] Nonappa,[2,3] Biswajit Mondal,[1] Kamalesh Chaudhari,[1] Heikki Rekola,[2†] Ville Hynninen,[3] Mauri A. Kostiainen,[4] Robin H. A. Ras, [3,4*] and Thalappil Pradeep[1*]*

[1]DST Unit of Nanoscience and Thematic Unit of Excellence, Department of Chemistry, Indian Institute of Technology Madras, Chennai 600036, India. [2]Faculty of Engineering and Natural Sciences, Tampere University, FI-33101, Tampere, Finland. [3]Department of Applied Physics, Aalto University, FI-00076 Aalto, Finland. [4]Department of Bioproducts and Biosystems, Aalto University, FI-00076 Aalto, Finland.

ABSTRACT

Directing the assembly of plasmonic nanoparticles into chiral superstructures has diverse applications including, chiroptical sensing, non-linear optics, and biomedicine. Though soft template-mediated assemblies of both spherical and non-spherical gold nanoparticles have made significant progress, most approaches require sophisticated chemical synthesis or advanced methodologies. Besides, reports of structurally precise chiral plasmonic assemblies beyond

nanoscale are limited. Here, we propose an efficient yet simple strategy to grow such precision assemblies up to mesoscale, which is beneficial for a broader community. Briefly, cationic gold nanorods (AuNRs) are allowed to systematically assemble along atomically-precise, chiral, rod-like tobacco mosaic virus (TMV) particles via electrostatic attraction under ambient condition. This leads to spontaneous formation of helical hybrid microwires with high structural precision, as evidenced by cryogenic transmission electron microscopy and tomography. Resulting composite superstructures show a strong circular dichroism response at the plasmon wavelength of the AuNRs, which is supported by simulations using discrete dipole approximation. Further, chirality of the system is investigated at a single microwire-level using polarized dark-field scattering microscopy. An alternative chiral template, negatively charged colloidal cellulose nanocrystals, also arrange AuNRs into similar chiral microstructures. Thus, our report proposes a generic methodology to obtain chiral plasmonic response at NIR region using inexpensive templates that will encourage the exploration of a wider range of nanoscale templates for creating hybrid mesostructures with emerging optoelectronic properties.

INTRODUCTION

Chirality is ubiquitous in nature and encountered at all length scales, from molecular-level to macroscopic objects. At molecular and macromolecular-level, biomolecules such as amino acids (except glycine), carbohydrates, proteins, and nucleic acids represent inherently chiral entities.[1] Further, at higher length scales, proteins (e.g., collagen and fibrin) and other biopolymers (e.g., agarose) undergo polymerization resulting in helical fibrillar nanostructures.[2] Importantly, chiral

entities absorb either right or left circularly polarized light preferentially (chiroptical properties). The differential absorption of right and left circularly polarized light leads to circular dichroism (CD).[3] CD spectroscopy is a powerful tool detecting molecular chirality,[4] protein folding-unfolding mechanisms and conformational changes during chemical reactions.[5] However, most chiral organic molecules absorb in the ultraviolet (UV) region, and signals are weak in the visible region of the electromagnetic spectrum. Selective functionalization of dye molecules with chiral substituents allow CD signals in the visible range of the spectrum.[6] Beyond the molecular level, chirality can also be amplified using self-assemblies to achieve helices, twisted tapes, or twisted ribbon-like nanostructures.[7]

Unlike organic molecules, metal nanoparticles possess the capacity to confine light, enhancing light-matter interaction. Many theoretical,[8, 9] and experimental,[10, 11] studies have shown that incorporation of plasmonic nanoparticles dramatically enhances the chiroptical response of a chiral system, thereby lowering its detection limit. They also serve as building blocks for optical metamaterials. Moreover, these plasmon-enhanced CD signals shift to the position of the plasmon resonance frequency of the respective nanoparticles, *i.e.* the visible-near-infrared (NIR) region.[12, 13] Thus, a broad wavelength range can be exploited simply by regulating the size and shapes of the nanoparticles. Such a phenomenon has application potential in circular polarizers,[14] detectors of circularly polarized light,[15] sensors of biomolecules[16] and asymmetric catalysis.[17] Therefore, strategies to efficiently conjugate plasmonic property and chirality have become an active field of research. Nanostructures with right- or left-handedness in their intrinsic morphology give highly intense CD signals. But they are either fabricated by a top-down approach like nanolithography, which has limitations in producing genuinely three-dimensional morphologies, especially in large-

scale production; or achieved through wet chemical syntheses, that are laborious, complex and suffer from non-uniformity and poor reproducibility.

Therefore, functionalization of commonly available spherical or anisotropic noble metal nanoparticles (NMNPs) with chiral moieties such as cysteine,[18] peptides,[19] polyfluorenes,[10] or DNA,[20] has evolved as a rather straightforward approach to induce chirality. Due to the interaction between these chiral molecules and the plasmon of the achiral nanoparticle, such composites show a prominent CD signal, which is called surface plasmon-enhanced circular dichroism (SPECD). From the numerous theoretical,[8, 21, 22] and experimental studies,[18, 19, 23] we can conclude that SPECD produces the strongest signal when chiral molecules are placed at the plasmonic hotspots within a 3D nanoparticle assembly. However, placing a single molecule in the hotspot with precision is challenging. Govorov and co-workers have shown that spherical gold nanoparticles, arranged in an asymmetric, *i.e.*, tetrahedral or helical geometry, produce a collective CD signal at their plasmonic resonance frequency.[21] Since then, a number of methodologies have been developed to arrange pre-synthesized NPs of desired size and shape along a soft helical backbone e.g., peptides,[24, 25] nematic liquid crystals,[26] fibre-like soft materials,[27] supramolecular backbones,[28] and DNA origami.[29, 30] The success of this strategy lies in the extent of precision by which the template can regulate the nanoparticles' three-dimensional arrangement. DNA origami, being programmable, serves as the most precise method for arranging NMNPs in a desired geometry.[31] However, the cost-intensive nature and high level of expertise required for DNA nanotechnology prohibit it from being the most useful strategy for materials scientists. Thus, although the field of template-assisted chiral plasmonic nanomaterials have made considerable progress, there is still room for a strategically simple way to assemble metallic nanoparticles on inexpensive soft templates with high structural precision. Bacterial cells[32] and viral capsids of

well-defined structures[33] are recently being explored as alternative building blocks of higher-level assemblies leading to functional nanomaterials. Simple electrostatic interactions can efficiently assemble protein cages within themselves,[34] as well as with plasmonic nanoparticles,[35] creating highly ordered superstructures. Keeping these in mind, we have chosen tobacco mosaic virus (TMV) as the chiral template. Native TMV is a biocolloidal substrate of rod-like morphology with known crystal structure, highly negative surface charge (zeta potential -25.4 mV in phosphate buffer of pH 7.8), and precise size and shape monodispersity. A viral RNA, helically wrapped by 2130 coat proteins, generates a right-handed chirality in its structure.[36] In the present work, we have allowed cationic AuNRs to arrange along the TMV surfaces through electrostatic self-assembly and observed a strong bisignate circular dichroism signal at the visible-NIR wavelength range. The generality of our strategy to create NIR chiral plasmonic microwires is established by using cellulose nanocrystals (CNC) as another template. DNA origami and peptide production technologies, though result in assemblies of high structural precision, are not easily scalable. On the contrary, extraction and purification procedures of TMVs and CNCs are well established in plant biotechnology allowing the production of these templates in kilograms. Moreover, for various device-based applications like telecommunication, significant effort has gone on to make mesoscale helical superstructures.[37] The morphology and surface charge distribution of TMV and CNC guide a spontaneous translation of chirality from nanoscale to micron scale range, which is a clear advantage of the present strategy. Thus, our approach addresses some of the most important challenges of achieving precision assembly of nanoparticles up to micron scale towards creating SPECD in the NIR region.

EXPERIMENTAL METHODS

Preparation and characterization of tobacco mosaic virus particles. The leaves of a month old *Nicotiana tabacum* (var. Samson) plants were inoculated by rubbing them with wild type TMV stock. The upper leaves that showed severe TMV symptoms, were collected after 22 days to achieve 52 g of leaf biomass. TMV was purified following the procedure reported by Chapman.[38] Precisely, 0.5M phosphate buffer of pH 7.2 along with 1% (v/v) 2-mercaptoethanol were used to homogenize the leaves. The leaf juice was filtered and extracted with butan-1-ol, centrifuged and the aqueous phase was collected. 4% PEG 8000 was used to precipitate the TMV. This pellet of virus was washed by phosphate buffer (10 mM, pH 7.2) mixed with 0.7M NaCl and 4% PEG. It was then resuspended and further purified according to Liljeström *et al*.[39] The stock TMV was diluted using DI water just before the experiments.

Synthesis of AuNR: Highly monodisperse gold nanorods of aspect ratio ~3.4 were obtained following a seedless synthetic procedure proposed by our group.[40] 20 mL of 100 mM CTAB solution was taken in a 50 mL conical flask and kept in a water bath to maintain the temperature at 28 °C. To this, 1 mL 10 mM $HAuCl_4.3H_2O$, 130 µL of 10 mM freshly prepared $AgNO_3$ and 140 µL 100 mM fresh ascorbic acid were added sequentially with mild stirring. As soon as the brownish yellow solution (due to the complex formed by CTAB and $HAuCl_4$) becomes colourless due to the reduction of Au^{3+} to Au^{+} by ascorbic acid, 200 µL of 1.67 mM $NaBH_4$, (freshly prepared in ice-cold water) was added at one shot. The stirring was stopped immediately after the addition of $NaBH_4$. Although the colourless solution slowly turns dark brown within 30 min showing the high yield of nanorods, it was kept undisturbed for at least 4 hours to ensure that the growth is complete.

Cationization of AuNRs. The excess CTAB-stabilized AuNRs were washed using distilled water for further use. For that, the as-synthesized AuNRs were taken in 2 mL plastic vials and centrifuged at 13000 rpm for 20 min, the supernatant from each vial was discarded, the precipitate was resuspended in 1.5 mL of DI water. This was again centrifuged in a similar way, but this time the precipitate was not resuspended in water. Rather, 20 µL of 4 mM ethanolic solution of (*11*-Mercaptoundecyl)-*N, N, N*-trimethylammonium bromide (MUTAB) was added to the pellet in each vial and it was shaken vigorously for initial 30 min. It was kept overnight without stirring and then washed with water. Precisely, the pellet was dispersed in 2 mL DI water, centrifuged, and then 1.9 mL water was decanted. Finally, it was dispersed in suitable amount of water to attain an absorbance of 1.2. such that the MUTAB concentration in the solution was significantly less than 0.002 mM.

Synthesis of CNCs: As described by Hynninen *et al*.,[41] Whatman grade 1 filter papers were ground to form a homogeneous powder. To 15 grams of this paper powder, 64% sulfuric acid solution was added in a round bottom flask and mixed thoroughly by stirring. This was hydrolysed at 45 °C for 45 min and then was diluted 10 times using milli-Q water to cease the reaction. This was kept still until complete sedimentation. The precipitate was collected after decanting the clear supernatant. The pellet was redispersed in milli-Q water and centrifuged at 6000 rpm for 20 min first and in the second round, at 2500 rpm for 45 min. Further purification was carried out by dialysis against milli-Q water until the conductivity of the dialysate reduced below 5 µS/cm. Now it was passed through a Whatman 541 filter paper and stored at +4 °C. The concentration of CNC was determined gravimetrically by slow evaporation of water and the stock solution was found to be 3.5 wt%.

TMV-AuNR$^+$ assembly formation: MUTAB-functionalized AuNRs were diluted by DI water until absorbance of the LSPR was ~1.2. The TMV stock solution was diluted using DI water to 0.21 mg/mL. 2 mL of this AuNR$^+$ was taken in the cuvette for UV-vis spectrometer, TMV was added at 25 uL steps and mixed gently using a pipette. After every addition, absorption spectra were measured to ensure systematic assembly from the slight gradual shift in the absorption peak maxima. There was no significant time gap needed between TMV addition and measurement of absorption spectra.

CNC-AuNR$^+$ assembly formation: This was the same as the assembly with TMV. CNC of 0.009 mg/mL concentration was added in 2 μL steps.

Instrumentation:

All the **UV-vis absorption spectra** were recorded using a PerkinElmer Lambda 25 UV-vis spectrometer.

The TEM measurements were performed using a JEOL 3010 (JEOL Japan) transmission electron microscope, using 200 kV acceleration voltage.

Serial EM and 3D reconstruction: For transmission Electron tomographic reconstruction, tilt series of 2D projections were acquired with the SerialEM software package.[42,43] Specimen was tilted between ±69° angles with 2° increment steps under low dose mode.[44] The acquired stack of images was first subjected for a series of pre-processing, coarse alignment, final alignment and further aligned using IMOD software package.[45] The final aligned file was then utilized for 3D reconstruction with custom made maximum entropy method (MEM) program with a regularization

parameter value of λ= 1.0e-3 on MacPro.[46] The 3D isosurface and solid coloured images were produced using UCSF Chimera.

Cryo-Transmission Electron Microscopy: The cryo-TEM images were collected using JEM 3200FSC field emission microscope (JEOL) operated at 300 kV in bright field mode with Omega-type zero-loss energy filter. Prior to sample preparation, 200 mesh copper grids with lacey carbon support film (Electron Microscopy Sciences) were plasma cleaned using Gatan Solarus (Model 950) plasma cleaner for 30 seconds. The samples for Cryo-TEM imaging were prepared by placing 3 µL of a of the sample on a plasma treated TEM grids and plunge-freezed into -170 °C ethane-propane (1:1) mixture using Leica automatic plunge freezer EM GP2 with 2 s blotting time under 100% humidity. The vitrified specimen was cryo-transferred to the microscope. The images were acquired with Gatan Digital Micrograph® software while the specimen temperature was maintained at -187 °C.

Circular dichroism study: The circular dichroism spectra of all the samples were measured in a Jasco J-1500 spectrometer. A quartz cuvette of 10 mm path length was used for each measurement.

Modelling the circular dichroism: We used the discrete dipole approximation (DDA)[47, 48] to calculate the CD signal for a nanoparticle assembly. The nanoparticle coordinates were determined from TEM tomography measurement, and the model contained 293 nanoparticles. The exact orientation of the nanorods could not be extracted from the tomography data, instead we had set the long axis of the nanorods along the main axis of the nanorod assembly with a normally distributed variance (sigma) of 20 degrees. The length of the nanorod was set to 34 nm with a variance of 6.2 nm, and the diameter to 10 nm with 2 nm variance. As the parameters had a

randomly generated component, all the results presented were average values obtained from 40 simulation runs.

In the simulations, each nanoparticle was represented by a point dipole. The polarizability of the point dipole was calculated using the modified long-wavelength approximation (MLWA),[49] assuming an ellipsoidal shape for the particle:

$$\alpha_{MLWA,j} = \frac{\alpha_j}{1 - \frac{k^2}{j}\alpha_j - \frac{2}{3}ik^3\alpha_j},$$

where α_j is the quasistatic polarizability of the particle along it's semiaxes $j = [a, b, c]$, given by

$$\alpha_j = 4\pi abc \frac{\varepsilon_1(\omega) - \varepsilon_2}{3\varepsilon_2 + 3L_j(\varepsilon_1(\omega) - \epsilon_2)}.$$

The term L_j is given by[50]

$$L_j = \frac{abc}{2}\int_0^\infty \frac{dq}{(q + j^2)\sqrt{(q + a^2)(q + b^2)(q + c^2)}}.$$

Finally, the polarizability of the nth nanoparticle of the structure is represented by a matrix

$$\alpha_n = \begin{pmatrix} \alpha_{MLWA,a} & 0 & 0 \\ 0 & \alpha_{MLWA,b} & 0 \\ 0 & 0 & \alpha_{MLWA,c} \end{pmatrix}.$$

This polarizability matrix was then rotated for each nanoparticle to account for the different orientations of the nanorods within the structure. Finally, we calculated the CD response of the self-assembled system using the discrete dipole approximation (DDA).[47,48] The induced dipole moments in the whole nanoparticle assembly were

$$\mathbf{P} = (\mathbf{1} - \hat{\boldsymbol{\alpha}}\mathbf{G}^{\mathbf{0}})^{-1}\,\hat{\boldsymbol{\alpha}}\mathbf{E}^{\mathbf{ext}}$$

We calculated the matrix inversion, and used it to evaluate the dipole moments for different incident fields $\mathbf{E_{ext}} = \mathbf{E}_k^{L/R}\exp(i\mathbf{k}\cdot\mathbf{r})$. Here the vector $\mathbf{k}$ was scanned over 100 different orientations on a unit sphere to obtain an average response of the structure to match the experiment

done in solution, and $\mathbf{E}_k^{L/R}$ defines the left- and right-handed polarizations for the corresponding **k**-value. From the dipole moments we calculated the extinction cross section as:

$$\sigma_{ext} = 4\pi k \sum_{j=1}^{N} \frac{\mathrm{Im}[\mathbf{E}^*_{ext,j} \cdot \vec{\mathbf{p}}_j]}{\left|\vec{\mathbf{E}}_{ext,j}\right|^2}$$

and the absorption cross section as[47]:

$$\sigma_{abs} = 4\pi k \sum_{j=1}^{N} \frac{1}{\left|\vec{\mathbf{E}}_{ext,j}\right|^2} \{\mathrm{Im}[\vec{\mathbf{p}}_j \left(\boldsymbol{\alpha}_j^{-1}\right)^* \vec{\mathbf{p}}_j^* - \frac{2}{3} k^3 \left|\vec{\mathbf{p}}_j\right|^2]\}$$

Finally, the circular dichroism signal was calculated from the cross sections as

$$\frac{\sqrt{\sigma_R} - \sqrt{\sigma_L}}{\sqrt{\sigma_R} + \sqrt{\sigma_L}}$$

Here, the subindices R and L corresponded to the two different circular polarizations.

RESULTS AND DISCUSSION

Cationization of AuNRs: Spherical nanoparticles of gold typically generate CD signals of moderate intensity over a narrow spectral range.[13, 24] On the contrary, AuNRs are capable of generating a much stronger electronic field owing to the anisotropic distribution of their free electrons.[31] Besides, their longitudinal surface plasmon resonance (SPR) frequency is highly sensitive towards their size, aspect ratio and electronic environment, i.e., the presence and orientation of neighbouring particles. Hence, AuNRs are promising building blocks for tunable

and intense CD signal. In an aqueous medium, cetyl trimethyl ammonium bromide (CTAB) molecules form a bilayer that covers the AuNRs. Although the zeta potential of CTAB-protected AuNR (AuNR@CTAB) is highly positive (+30 mV) due to the quaternary amine group of CTAB, there is no covalent bond between the gold atoms and the CTAB molecules, making the protective layer labile. Therefore, using a typical ligand exchange method, we functionalized the AuNRs with a thiol containing positively charged end group and a chain length comparable to that of CTAB, namely (*11*-Mercaptoundecyl)-*N, N, N*-trimethylammonium bromide (MUTAB). The Au-S bond formation facilitated the replacement of CTAB bilayer by MUTAB molecules, producing MUTAB-protected AuNRs, which is abbreviated here as $AuNR^+$ (Figure 1a, Figure S1). The TEM image of $AuNR^+$ (Figure 1b) and the distribution of their length and diameter (Figure 1c) suggest uniform shape and narrow size dispersity, the mean length being 34±4.5 nm and mean diameter being 10±1.2 nm (aspect ratio ~3.4). The 3D reconstruction of a single $AuNR^+$ morphology using electron tomography is shown in Figure 1d and Video S1. Its comparison with that of AuNR@CTAB (Figure S2) further shows that the morphology was intact on ligand exchange. Comparing the absorption spectra of AuNR@CTAB and $AuNR^+$ (Figure 1e), it can be concluded that the ligand exchange did not alter the dispersity and electronic environment of the as-synthesized AuNRs. The resulting $AuNR^+$ retained its cationic nature as suggested by its positive zeta potential (+18 mV).

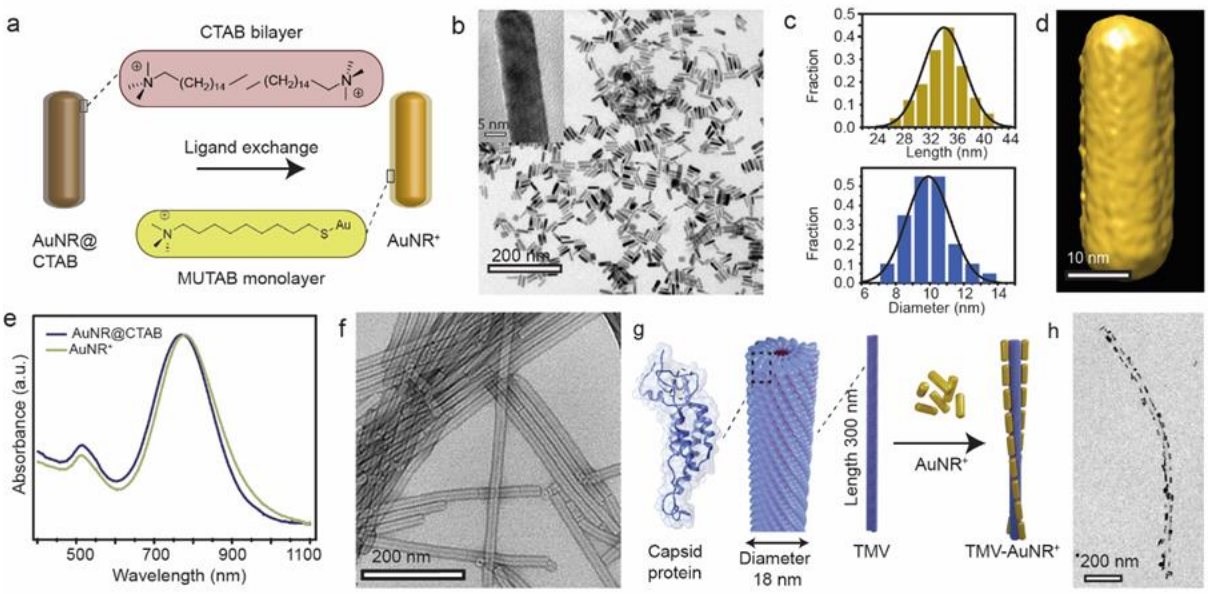

Figure 1. Starting materials and product of the electrostatic assembly. (a) Schematic of the functionalization of AuNR@CTAB with MUTAB via ligand exchange method, (b) TEM image of $AuNR^+$, (c) distribution of length and diameter of 200 $AuNR^+$s measured from the TEM images, and (d) TEM-tomographic image of a single $AuNR^+$. (e) Comparative absorption spectra of AuNRs before and after MUTAB functionalization, (f) TEM image of negatively stained TMVs. (g) Cartoon representation of the TMV structure and the schematic presentation of the electrostatic interaction between TMV and $AuNR^+$, and (h) TEM image of resulting TMV-$AuNR^+$ composite.

Assembly of $AuNR^+$ on TMV: TMV is an anisotropic biocolloidal substrate with a radius of 18 nm and length of 300 nm (Figure 1f).[36] The virus is semiflexible, atomically precise, and therefore, highly suitable as a soft template for drug delivery,[51] ordered assemblies of chromophores,[52] nanoparticles[53] and deposition of metal ions.[54] The crystal structure of TMV reveals that there are 130 turns of the coat proteins along the length of a single TMV causing a spiral negative charge distribution on the surface.[55] Therefore, cationic $AuNR^+$ got adhered on the TMV guided by the strong electrostatic attraction. In case of such assemblies, the relative position of adjacent

nanoparticles has great influence on the final structure and properties of composite materials. Moreover, nanorods being anisotropic in morphology, the relative angles between the longitudinal axes of $AuNR^+$s within themselves and between $AuNR^+$s and TMVs act as another crucial parameter while they form a binary assembly. Previously, it has been observed that AuNRs have a tendency to follow the orientation of anisotropic templates.[56] In this case also directional synergy played an important role which led the $AuNR^+$s to attach to the TMV particles keeping their longitudinal axis almost parallel to that of the TMV. This structure was also favoured by the maximum attraction between cationic $AuNR^+$ and anionic TMVs. Figure 1g represents the electrostatic assembly schematically and Figure 1h shows a TEM image of the resulting TMV-$AuNR^+$ composite. Notably, the $AuNR^+$ aligned themselves in stripes on opposite sides of the cylindrical TMV rather than covering their entire surface evenly, as observed previously by Liz Marzan's group in case of carbon nanotube template.[57] The perfectly cylindrical shape of TMV led to the end-to-end arrangement of $AuNR^+$s without any defect (misalignment of rods) enabling greater uniaxial plasmon coupling.

Long-range assembly of TMV-$AuNR^+$: TMVs are well-dispersed in the aqueous medium, owing to their high negative surface charge. However, they are known to form 2D hexagonally close-packed bundles under certain conditions.[58, 59] Stoichiometric ratio of the two constituents is crucial for a binary assembly. Hence, to study the assembly at different stoichiometric ratios of $AuNR^+$ and TMV, the latter was added stepwise to 0.16 nM $AuNR^+$ solution and analysed after each addition. The volume of TMV solution was too small (final dilution was 5%) to significantly alter the $AuNR^+$ concentration in the medium. Figure 2a shows the change in the absorption spectrum of $AuNR^+$ during the process. Longitudinal surface plasmon resonance (LSPR) band of $AuNR^+$, i.e., the one appearing at the longer wavelength (here at ~770 nm), is known to be more

sensitive towards any change in the system compared to the transverse surface plasmon resonance (TSPR) band at 520 nm. In agreement, we observed a gradual redshift of the LSPR peak maximum with increasing concentration of TMV along with a decrease in the value of absorbance, peak broadening and rise in the baseline. The redshift implies plasmonic coupling among the $AuNR^+$s in the longitudinal direction. As a control experiment, a comparable concentration of MUTAB was added to native TMV and TEM image of them revealed that it did not induce any specific interaction among TMVs (Figure S3a). Now, at low TMV concentration, we observed that some of the $AuNR^+$ assembled along the TMVs and excess $AuNR^+$ was found to remain dispersed in the medium (Figure S3b). With increase in the TMV concentration, more and more $AuNR^+$ took part in the binary assembly. The resulting LSPR peak broadened as it was now having contributions from both free $AuNR^+$ (LSPR at ~770 nm) as well as $AuNR^+$s arranged on to the TMV surfaces (LSPR at > 770 nm). These two factors, together with the rise in the baseline, indicate the abundance of TMV-templated assembly of $AuNR^+$ to higher-order structures in the medium. Figure 2b-d show the TEM images of the resulting composite structures in the presence of 2, 6 and 10 μg/mL TMV, respectively. The electron microscopy images suggest that as the concentration of TMV increases, the discrete TMV-$AuNR^+$ units containing one TMV each, acted as the nucleating sites and excess TMV and $AuNR^+$ participated in further assembly leading to a long-range structure. Owing to the complementary hydrophobic interactions between the dipolar ends of the helical structure, TMVs are known to take part in a head-to tail assembly.[60] In accordance, initially the TMV-$AuNR^+$ structures grew longitudinally much more than in the transverse direction, as shown in Figure 2b. Unidirectional assembly of native TMVs is favoured as this minimizes the repulsion between the carboxylic residues at the assembly interface. But

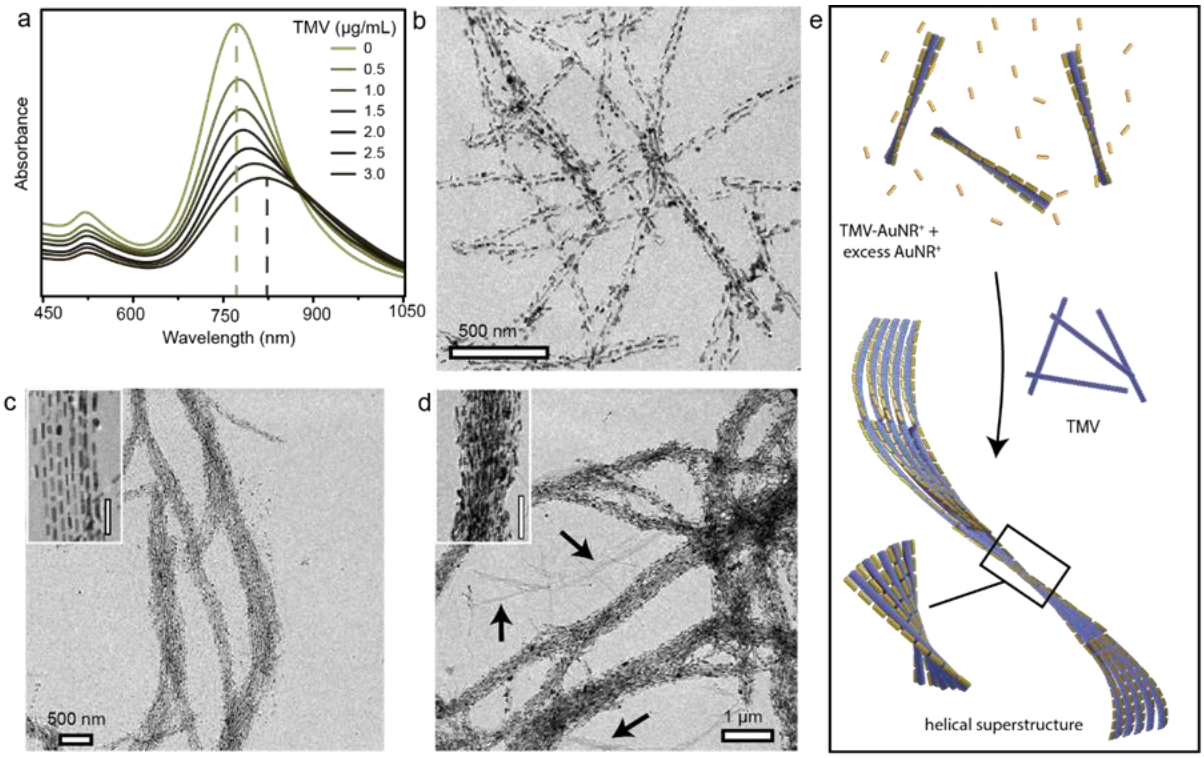

Figure 2. Long-range assembly of TMV-AuNR$^+$s. (a) Change in the absorption spectra of AuNR$^+$ (0.16 nM) with gradual TMV addition, (b) TEM image of the assembly at 2 μg/mL TMV, (c) TEM image of the assembly at 6 μg/mL TMV showing ribbon-like morphology; magnified image in the inset reveals its 2D superlattice (scale bar 50 nm). (d) TEM image of a bundle-like assembly at 10 μg/mL TMV; magnified image in the inset shows 3D superlattice (scale bar 500 nm) and the arrows point to the excess TMVs. (e) Schematic of the assembly formation.

upon AuNR$^+$ attachment, the negative surface charge of TMVs were neutralized. Therefore, growth of the assembly in the transverse direction also became feasible. This process maximized the attractive force between the two components with opposite surface charges and minimized the repulsive force between similar surface charges. As shown in Figure 2c, gradually it took the shape of a ribbon, showing an ABAB... arrangement along the width, where A=TMV and B=linear array of AuNR$^+$. The inset in Figure 2c presents a magnified view revealing the 2D superlattice domains

of these superstructures. Figure 2e schematically presents the long-range assembly. With further increase in the TMV concentration, due to overgrowth, this 2D ribbon-like superstructure attained thick wire-like morphology with 3D bundled superlattice structures (as shown in Figure 2d). Beyond this point, addition of TMV only made these wires thicker and longer without any significant morphological change. Finally, these several microns-long wires started to precipitate and excess free TMV can be observed in the corresponding TEM images.

Origin of the helical structure leading to plasmonic chirality: From Figure 2 it is evident that the long and thick TMV-AuNR$^+$ superstructures contain hints of structural twists in the long-range. To eliminate any drying artifact, we characterized this binary superstructure under cryogenic conditions. Although the periodic array of TMVs and AuNR$^+$ appear parallel locally (inset in Figure 2c), the cryo-TEM image in Figure 3a shows that the ribbon-like TMV-AuNR$^+$ composite wires indeed show helicity in their structure. A magnified image displays that it is completely twisted at places. Using a tilt series of images, we reconstructed a 3D structure of this wire (Figure 3b, Video S2) which presents a clearer view. The origin of this helicity lies in the crystal structure of TMV, where a right-handed RNA helix is buried inside the capsomeres. These capsomeres show an axial repeat distance of 69Å, which consists of 49 subunits while the basic helix makes three turns. Previous studies have shown that chiral rod-shaped viruses align in a twisted fashion with each other to minimize their interaction energy.[61] In this case, the net effect of a strong attraction between AuNR$^+$ and TMV and the helical distribution of negative charge along the TMV surface gave rise to the helicity in the superstructure. In a study by Liljeström *et al.*,[39] spherical cationic gold nanoparticles, in a high electrolyte concentration were mixed with TMV and the mixture was dialysed. This way, instead of any kinetically driven random electrostatic assembly, the authors

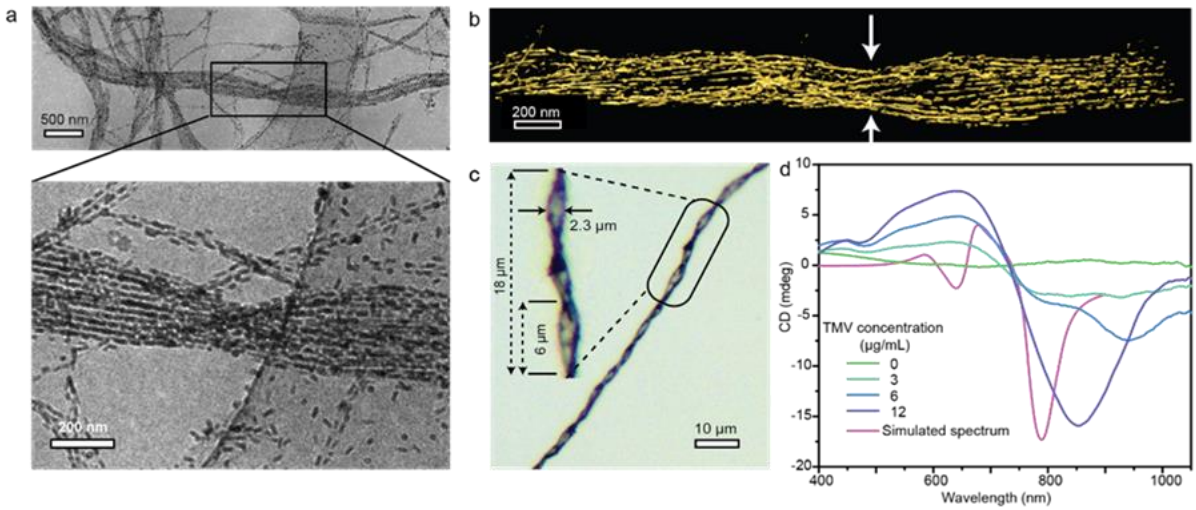

Figure 3. Plasmonic chirality of the TMV-AuNR$^+$ wires. (a) Cryo-TEM image of a ribbon-like TMV-AuNR$^+$ superstructure along with the magnified view of a twisted section; (b) corresponding 3D reconstructed image with arrows pointing to the helical twist, c) optical image of a TMV-AuNR$^+$ microwire in presence of 12 µg/mL TMV showing repetitive twists. Magnified view of the marked section shows the pitch-length. (d) Experimental CD spectra showing stronger signals with gradually higher TMV concentration, along with the simulated CD spectrum calculated from the AuNR$^+$ coordinates obtained from image (b).

obtained a highly ordered ribbon-like superstructure through a zipper-like mechanism. Furthermore, the superstructure showed helicity, generating CD signal around the plasmon wavelength of AuNPs. The success of this strategy lies in the colloidal stability of the AuNPs against the electrolyte. However, in some cases the plasmonic nanoparticles tend to aggregate irreversibly even at a moderate salt concentration. The present study addresses this limitation. We show that fairly ordered helical superstructures can be achieved by slow stepwise addition of the chiral template to the pool of AuNR$^+$, without the risk of electrolyte treatment. We also notice that the helicity became more prominent with the growth of the superstructure. Figure 3c presents

optical microscopy image of a composite ribbon-like structure that is several hundreds of microns in length and up to 2.3 μm in width. Periodic structural twists can be seen along the entire micro-wire. Inset shows a magnified view of the marked portion which reveals a pitch of 6 μm. Optical images of the system at various TMV concentrations in Figure S4 show that at lower TMV concentration, the structures contained occasional twists. Whereas, at TMV concentrations higher than 12 μg/mL, the pitch increased with the width of the microwires (Figure S4b-c). Thus, through the self-assembly process, the molecular level chirality was transposed to the chiral structures of multiple orders of magnitude larger length scales. Notably, in the proposed mixing protocol, we hypothesize that each structural units of the template got saturated by $AuNR^+$ before more templates entered into the system. However, when we performed the reverse addition process, *i.e.*, gradually added small amount of $AuNR^+$ to an aqueous solution of TMV, the former chose random structural units of TMV to attach to. This continued, making the subsequent long-range assembly impossible. In the cryo-TEM images, we see that the assembly didn't continue beyond a few TMV-$AuNR^+$ units (Figure S5).

Besides, the circular dichroism measurements reveal that the structural helicity of the micro-wires had a preferred handedness that gave rise to an overall chirality. In Figure 3d we see that the system gives a bisignated CD signal of peak-dip feature with a zero-crossing point around the absorption maximum of the $AuNR^+$. This nature of the CD spectra is typical for helical plasmonic assemblies. Here, although the $AuNR^+$s arranged on the surface of TMV in near-parallel 1-D arrays, the right-handed distribution of surface charge on TMV guided the assembly to finally give the right-handed global twists. As explained in detail in the previous study with gold nanoparticles by Liljeström *et al.*,[39] if one observes from the transverse direction, the nanorods show a left-handed arrangement which gives the peak-dip type CD signal. In solution, the experimental CD spectra are the average

of chiral signals coming from the axial as well as transverse directions of the TMV-AuNR$^+$ composite microwires. Now, considering the micron scale length of the wires, any light propagating along their longitudinal axis would be heavily damped by the gold nanorods, decreasing the contribution of this orientation in the experimental CD. Therefore, the left-handed arrangement from the transverse direction predominates and the resulting signal follows the peak-dip nature. A similar CD signal was also reported by Nicholas A. Kotov's group for ribbon-like chiral plasmonic composite structures.[62].

As predicted from the electron microscopy and optical images, with higher TMV concentration in the medium, the CD signal became stronger in both positive and negative sides while keeping the baseline and the zero-crossing position almost constant. Beyond a certain TMV concentration (12 μg/mL of TMV), as the wires became too heavy to stay dispersed in the aqueous medium, the bulk CD spectrum got flattened (Figure S6). To avoid dependency of chirality on concentration, asymmetry factor or g-factor of the system was calculated from these CD spectra and corresponding absorbance spectra at different TMV concentrations following the usual method.[63] As shown in Figure S6c, a prominent peak-dip trend of the spectrum was observed for 12 μg/mL TMV concentration that shows a standard value for this kind of systems.[62] Using the CD data and corresponding absorbance values from Liljeström *et al*.,[61] g-factor of TMV-gold nanoparticle system at 200 mM salt concentration is also plotted in Figure S6d. Both the systems show comparable negative peak intensity, but a much stronger (~10 times higher) positive signal in case of TMV-AuNR$^+$ suggests better chiral response in case of AuNR$^+$. Taking the position of the AuNR$^+$s in the assembly from the coordinates of its cryo-TEM tomogram and using the discrete dipole approximation (DDA) we simulated the CD signal of the TMV-AuNR$^+$ microstructure shown in Figure 3b. The model contains 293 nanorods, each represented as a point dipole, with

polarizability obtained from the modified long-wavelength approximation (MLWA). Taking the length of the nanorods as 34±6 nm and the diameter as 10±2 nm (for details see methods), we obtain the CD spectrum presented along with the experimental spectra in Figure 3d. The zero-crossing position of this simulated spectrum matches well with our experimental result, the signal intensity being comparable with the one when the TMV concentration was 12 μg/mL. The sharpness of the simulated CD spectrum can be attributed to the fact that the model takes coordinates from the cryo-tomographic image of a single structure. However, in solution (as shown in Figure 3a), the length and width of the micro-wires vary to some extent, which contribute to the broadening of bulk CD spectra. The experimental spectra are smoothened and the simulated spectrum is multiplied by a simple integer for ease of comparison.

Chirality estimation at single microwire level: Owing to its ensemble-averaging nature, bulk CD measurements often mask the sensitivity of CD spectroscopy. Therefore, researchers are taking a growing interest in detecting chirality at single particle level using far-field extinction microscopy[64] and single particle chiral scatterometry.[65] Using a much simpler technique, namely, polarized dark field scattering microspectroscopy (PDFSMS), we have determined the chirality associated with individual composite TMV-AuNR$^+$ microwires. PDFSMS allows detection of chirality associated with individual gold nanorod aggregates both qualitatively as well as quantitatively.[66] This is possible because of the optical rotation due to plasmonic circular dichroism of the anisotropic nanoparticle assemblies. Here, using the same principle and experimental set-up, we studied chirality associated with individual TMV-AuNR$^+$ microwires. Precisely, we used an upright dark field microscope to image TMV-AuNR$^+$ sample placed between a glass slide and a glass-coverslip. Depending on the TMV to AuNR$^+$ ratio we observed dot-like, rod-like and wire-like structures (Figure S7). Figure 4a shows a dark-field optical image of the

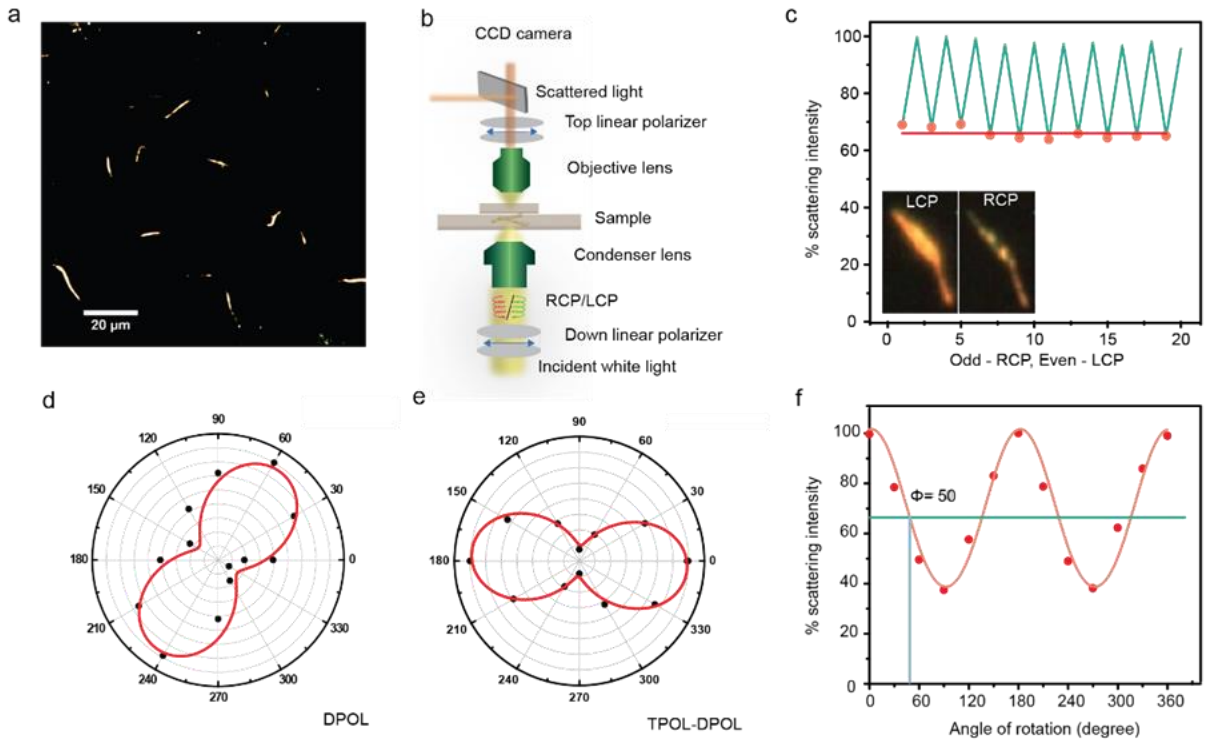

Figure 4. Chirality study of single microwires. (a) Dark-field optical image of the composite wires made of TMV-AuNR^{+}, (b) schematic representation of the PDFSMS set up, (c) changes in the scattering intensity of a single microwire (inset shows the images) when it was illuminated with RCP and LCP alternatively and observed through analyzer. (d) Polar map of a single wire when it was illuminated with a linearly polarized light at different angles (0-360°) without analyzer and (e) with analyzer. (f) The polar plot in (e) presented as 2D XY plot to find the angle of optical rotation of a microwire.

sample containing 6 μg/mL TMV in the absence of any polarizer. Now we modified the set up as shown in Figure 4b such that the sample could be illuminated with right and left-handed circularly polarized light and optical rotation in the light scattered by the microwires could be detected. For this, a linear analyzer was added in the path of scattered light. Figure 4c shows changes in the average grayscale intensity for one of the microwires (inset, Figure 4c) upon alternate illumination

with RCP and LCP light. This plot shows repeatability of the measurements as well as reveals that upon changing the illumination from LCP to RCP, the scattering intensity passing through analyzer is reduced to 65%. Such alteration of intensity proves that the individual microwires are chiral, as expected from their twisted structures. To quantify the chirality of microwires results into the optical rotation of scattered light. Precisely, to illuminate the sample with linearly polarized light at different angles, we kept a linear polarizer at the bottom of the sample (down side polarizer, *i.e,* DPOL). Now, dark field images were collected without and with analyzer, *i.e.,* another linear polarizer kept above the sample (top side polarizer, *i.e.*, TPOL). These data are shown in Figure 4d and 4e, respectively. Then the percentage reduction in scattering intensity (65%) due to the optical rotation was correlated with the changes in the linearly polarized scattering intensity upon varying angle of linearly polarized illumination. It showed that when illumination is changed from LCP to RCP, the scattered light rotates by 50 degrees, which is a measurement of the optical rotation exhibited by the corresponding microwire. Notably, in aqueous dispersion, differential absorption for RCP and LCP was observed, but not optical rotation as the TMV-AuNR^{+} wires were oriented in all possible directions. Hence, output could be only circular and unpolarized light; and thus, bulk circular dichroism spectra were not affected by linear dichroism components.

Generalization of the strategy using cellulose nanocrystals (CNC): To show the generic nature of this approach, we used anisotropic nanocellulose particles viz. CNC. Cellulose is found in many skeletal systems of plants, mostly in a chiral nematic liquid crystal phase. Below a critical concentration, a form of cellulose exists as a whisker-like colloidal substance[67] with an average aspect ratio of 12, known as CNC, whose cryo-TEM images shown in Figure 5a. These rod-like CNCs contain sulfate half-ester groups on their surface and have a right-handed twisted structure[68]

which results in a helical distribution of negative surface charge similar to that of TMVs. Though these are not atomically precise, they are highly crystalline, the surface contains negatively charged groups (zeta potential -64 mV), and most importantly, these are highly abundant, and therefore even cheaper in cost. Earlier, CNCs have shown the potential to serve as a chiral template both in its nematic phase[69] and as single crystals.[70] Here, we added 0.02 wt% of colloidal CNC at each step to 0.16 nM $AuNR^+$ solution following the same strategy. As depicted in Figure 5b, the $AuNR^+$s attached to the CNC surface keeping their longitudinal axis parallel to that of the CNCs.

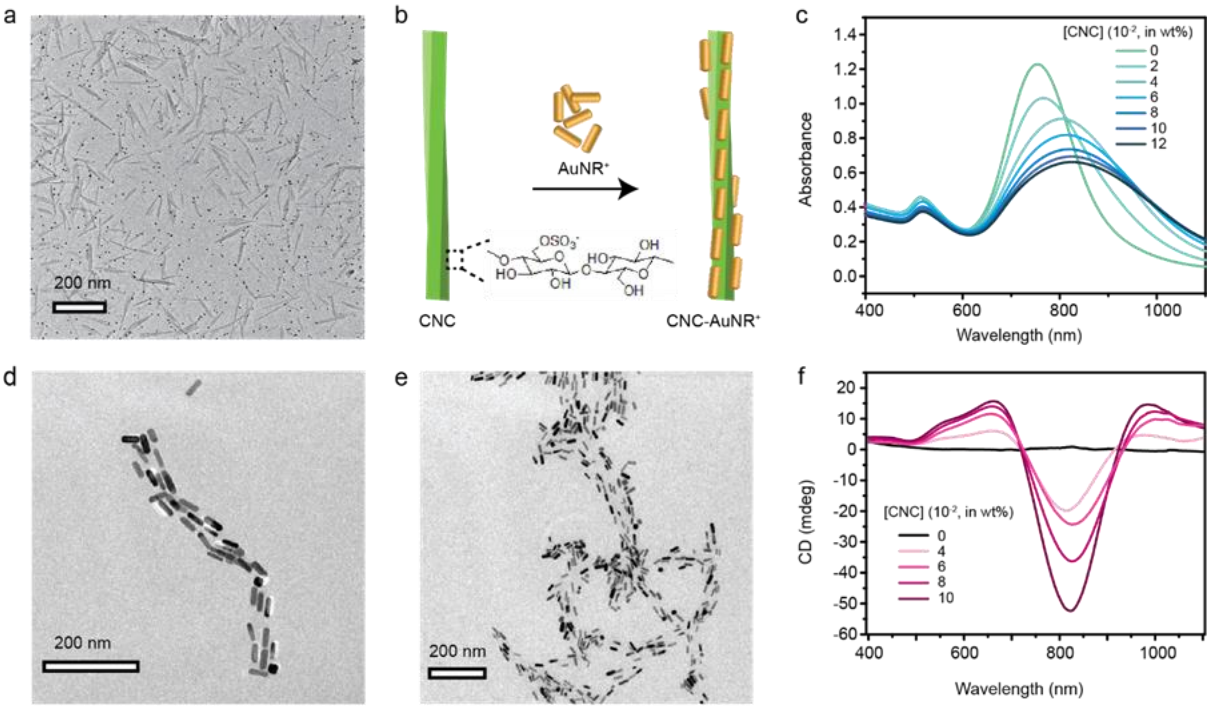

Figure 5. Long-range assembly of $AuNR^+$ with CNC. (a) Cryo-TEM image of negatively stained CNCs, (b) schematic of the arrangement of $AuNR^+$ on twisted CNC surface, (c) change in the absorption spectrum of $AuNR^+$ with gradual addition of CNC. (d) TEM image of short-range assembly at 0.02 wt% of CNC, (e) that of long-range assembly at high CNC concentration (~0.06 wt%), and (f) CD spectra of the sample with increasing CNC concentrations.

Notably, in this case, they attached to the CNCs covering their entire surface. During the process, the positive zeta potential of the system kept on decreasing (Figure S8), suggesting surface charge neutralization through electrostatic assembly. Figure 5c shows that the absorption spectra gradually shift towards the right and get broadened verifying a similar interaction as expected from the TMV's case. Indeed, the TEM image of the sample at low CNC concentration (Figure 5d) suggests that the $AuNR^+$s arranged themselves unidirectionally along the length of the CNC. At higher concentration of CNC, a long-range assembly produced longer and thicker composite structures. In Figure 5e we see such an assembled structure where, although the CNCs are hardly visible due to low contrast, the pattern of $AuNR^+$ arrangement clearly indicates that they were longitudinally attached to an anisotropic soft template of higher aspect ratio. Circular dichroism study shows that CNC-$AuNR^+$ also produced a chiral signal at the position of the maximum absorption of $AuNR^+$. Similar to the case of TMV, with the increase in the concentration of CNC, as the microstructures grew, the system showed stronger chiral signal keeping the zero-crossing position fixed. In case of CNC, the template is not perfectly cylindrical like TMV, but they rather contain right-handed structural twist in their inherent geometry. Therefore, CNC-$AuNR^+$ composite did not produce ribbon-like ordered structure with global twists. Instead, the nanorods evenly covered the CNC surfaces, guided by the grooves of CNCs. Several studies have shown that dihedral angle between nanoparticles significantly alter their chiral response.[71] Although less ordered, the CNC-$AuNR^+$ assemblies contained higher relative angle between consecutive gold nanorods compared to their uniaxial end to end arrangement in TMV-$AuNR^+$ system, which gives rise to a stronger CD signal in case of CNC-$AuNR^+$.

Calculated g-factor of CNC-$AuNR^+$ implies that the chiral response of this system is comparable with that of TMV-$AuNR^+$ (Figure S9). Notably, the spectra fail to show stronger signal intensity

with the increase in CNC concentration beyond 0.06 wt% of CNC. This can be attributed to the fact that CNC-templated assemblies of $AuNR^+$ show greater polydispersity leading to a flattening of the absorbance spectra (as evident from Figure 5c). However, the strong CD spectra and standard g-factor values imply that our strategy works well for CNC too, which may be extended to any template of this kind.

CONCLUSION

In the field of template-assisted plasmonic chirality, we present a simple strategy to obtain a binary assembly with structural precision. Using surface chemistry as a key, by slow stepwise addition of the rod-shaped chiral templates to a large pool of well-dispersed AuNRs, we observed systematic attachment of the AuNRs to the templates following their structural helicity. With gradual increase in the template concentration in the system, these unit composite structures participate in a long-range assembly that gives longer, thicker wire-like structures with an overall structural chirality. Thus, by following the proper mixing protocol, without any sophisticated template or complex sample preparation technique or highly specialised and tedious chemical synthesis, we can create structures that show plasmonic chirality at the NIR wavelength region. Besides being simple and general in nature, this method is highly reproducible, easily scalable, and efficient for tuning the length of the structures (Figure 2c-e), thereby bridging between nanoscale and microscale structural chirality. Interestingly, although both TMV and CNC-templated assemblies of $AuNR^+$ give rise to plasmonic chirality around the same wavelength following the same strategy, they may be suitable for very different applications. If the radiative and non-radiative losses can be minimized, the several-microns-long chiral plasmonic wires made of TMV-$AuNR^+$ might have potential utility in non-linear optics, and in telecommunication kind of devices. They can also be

excellent waveguides to preferentially propagate one circularly polarized light over the other, due to their chirality. On the other hand, the CNC-AuNR$^+$ system does not give such long unidirectional structures, but at high concentration of CNC, they show stronger signal in CD spectra (Figure 5f). Hence, CNC-AuNR$^+$ system would be more suitable for other applications where strong chirality in the NIR region is crucial. Further, using PDFSMS we could detect the chirality of a single TMV-AuNR$^+$ composite microwire. This method has the potential to detect TMV or similar chiral templates with an unprecedented detection limit. Thus, the chiral plasmonic materials proposed in this study hold importance to diverse field of physics, chemistry, material science and biology.

ASSOCIATED CONTENT

Supporting Information

The following files are available free of charge.

Additional characterization of AuNR before and after MUTAB functionalization, TEM images of TMV-AuNR$^+$ in presence of low TMV concentration, scanning electron micrograph, polarized optical image and dark-field optical images of TMV-AuNR$^+$, cryo-TEM images of TMV-AuNR$^+$ resulting from reverse addition, raw circular dichroism spectra of TMV-AuNR$^+$ at various TMV concentrations, change in zeta potential of CNC-AuNR$^+$ system with increasing CNC concentration (PDF)

Tomographic reconstruction of AuNR$^+$ (AVI)

Tomographic reconstruction of TMV-AuNR$^+$ (AVI)

AUTHOR INFORMATION

Corresponding Authors

Thalappil Pradeep − Department of Chemistry, DST Unit of Nanoscience (DST UNS) and Thematic Unit of Excellence (TUE), Indian Institute of Technology Madras, Chennai 600 036, India; orcid.org/0000-0003-3174-534X; Email: pradeep@iitm.ac.in

Robin H. A. Ras − Department of Applied Physics, and Department of Bioproducts and Biosystems, Aalto University, FI-00076 Aalto, Finland. Email: robin.ras@aalto.fi

Mauri A. Kostiainen − Department of Bioproducts and Biosystems, Aalto University, FI-00076 Aalto, Finland. Email: mauri.kostiainen@aalto.fi

Authors

Amrita Chakraborty – *DST Unit of Nanoscience (DST UNS) and Thematic Unit of Excellence (TUE), Department of Chemistry, Indian Institute of Technology Madras, Chennai 600 036, India.*

Nonappa – *Department of Applied Physics, Aalto University, FI-00076 Aalto, Finland and Faculty of Engineering and Natural Sciences, Tampere University, FI-33101, Tampere, Finland.*

Biswajit Mondal – *DST Unit of Nanoscience (DST UNS) and Thematic Unit of Excellence (TUE), Department of Chemistry, Indian Institute of Technology Madras, Chennai 600 036, India.*

Kamalesh Chaudhari – *DST Unit of Nanoscience (DST UNS) and Thematic Unit of Excellence (TUE), Department of Chemistry, Indian Institute of Technology Madras, Chennai 600 036, India.*

Heikki Rekola – *Faculty of Engineering and Natural Sciences, Tampere University, FI-33101 Tampere, Finland.*

Ville Hynninen – *Department of Applied Physics, Aalto University, FI-00076 Aalto, Finland.*

Present Addresses

†Current address: Department of Mathematics and Physics, University of Eastern Finland, FI-80101

Joensuu, Finland.

Author Contributions

A. C., T. P., M. A. K and R. H. A. R. conceived of the experimental design. A. C. prepared the samples and performed UV−vis studies and CD spectroscopy. N. performed cryo-TEM sample preparation and imaging, electron tomography reconstruction and image analysis. B. M. collected TEM images. K. C. performed the PDFSMS study. H. R. carried out theoretical modelling of the CD spectrum. V. H. synthesized the CNCs. A. C. and N. wrote the first draft of the manuscript and the final version of the manuscript was prepared through the contributions of all authors.

ACKNOWLEDGMENT

We thank the Department of Science and Technology, Government of India and the Academy of Finland (Project 308578), HYBER Centre of Excellence Programme (2014–2019) and Photonics Research and Innovation (PREIN) flagship for supporting our research. A. C. and B. M. thank the Council of Scientific and Industrial Research and IIT Madras, respectively for their research fellowships. We acknowledge the provision of facilities and technical support by Aalto University

at OtaNano-Nanomicroscopy Center (Aalto-NMC). We also thank Prof. Anton Kuzyk and Ryssy Joonas for their support in circular dichroism measurements.

REFERENCES

1. Blackmond, D. G. The origin of biological homochirality. *Cold Spring Harb. Perspect. Biol.* **2010,** *2*, a002147.

2. Runnels, C. M.; Lanier, K. A.; Williams, J. K.; Bowman, J. C.; Petrov, A. S.; Hud, N. V.; Williams, L. D. Folding, Assembly, and Persistence: The Essential Nature and Origins of Biopolymers. *J. Mol. Evol.* **2018,** *86*, 598-610.

3. Ranjbar, B.; Gill, P. Circular Dichroism Techniques: Biomolecular and Nanostructural Analyses- A Review. *Chem. Biol. Drug Des.* **2009,** *74*, 101-120.

4. Nakanishi, K.; Berova, N.; Woody, R. *Circular Dichroism: Principles and Applications*. VCH: New York, 1994; pp 230.

5. Kelly, S. M.; Jess, T. J.; Price, N. C. How to study proteins by circular dichroism. *Biochim. Biophys. Acta - Proteins. Proteomics.* **2005,** *1751*, 119-139.

6. Palmans, A. R. A.; Meijer, E. W. Amplification of Chirality in Dynamic Supramolecular Aggregates. *Angew. Chem. Int. Ed.* **2007,** *46*, 8948-8968.

7. Liu, M.; Zhang, L.; Wang, T. Supramolecular Chirality in Self-Assembled Systems. *Chem. Rev.* **2015,** *115*, 7304-7397.

8. Govorov, A. O. Plasmon-Induced Circular Dichroism of a Chiral Molecule in the Vicinity of Metal Nanocrystals. Application to Various Geometries. *J. Phys. Chem. C* **2011,** *115*, 7914-7923.

9. Ben-Moshe, A.; Maoz, B. M.; Govorov, A. O.; Markovich, G. Chirality and chiroptical effects in inorganic nanocrystal systems with plasmon and exciton resonances. *Chem. Soc. Rev.* **2013,** *42*, 7028-7041.

10. Oh, H. S.; Liu, S.; Jee, H.; Baev, A.; Swihart, M. T.; Prasad, P. N. Chiral Poly(fluorene-alt-benzothiadiazole) (PFBT) and Nanocomposites with Gold Nanoparticles: Plasmonically and Structurally Enhanced Chirality. *J. Am. Chem. Soc.* **2010,** *132*, 17346-17348.

11. Hentschel, M.; Schaeferling, M.; Duan, X.; Giessen, H.; Liu, N. Chiral plasmonics. *Sci. Adv.* **2017,** *3*, e1602735.

12. Lieberman, I.; Shemer, G.; Fried, T.; Kosower, E. M.; Markovich, G. Plasmon-Resonance-Enhanced Absorption and Circular Dichroism. *Angew. Chem. Int. Ed.* **2008,** *47*, 4855-4857.

13. Wang, Y.; Xu, J.; Wang, Y.; Chen, H. Emerging chirality in nanoscience. *Chem. Soc. Rev.* **2013,** *42*, 2930-2962.

14. Gansel, J. K.; Thiel, M.; Rill, M. S.; Decker, M.; Bade, K.; Saile, V.; von Freymann, G.; Linden, S.; Wegener, M. Gold Helix Photonic Metamaterial as Broadband Circular Polarizer. *Science* **2009,** *325*, 1513.

15. Hodgkinson, I.; Wu, Q. h. Inorganic Chiral Optical Materials. *Adv. Mat.* **2001,** *13*, 889-897.

16. Hendry, E.; Carpy, T.; Johnston, J.; Popland, M.; Mikhaylovskiy, R. V.; Lapthorn, A. J.; Kelly, S. M.; Barron, L. D.; Gadegaard, N.; Kadodwala, M. Ultrasensitive detection and characterization of biomolecules using superchiral fields. *Nat. Nanotechnol.* **2010,** *5*, 783-787.

17. Tang, Y.; Cohen, A. E. Enhanced Enantioselectivity in Excitation of Chiral Molecules by Superchiral Light. *Science* **2011,** *332*, 333.

18. Shukla, N.; Bartel, M. A.; Gellman, A. J. Enantioselective Separation on Chiral Au Nanoparticles. *J. Am. Chem. Soc.* **2010,** *132*, 8575-8580.

19. Slocik, J. M.; Govorov, A. O.; Naik, R. R. Plasmonic Circular Dichroism of Peptide-Functionalized Gold Nanoparticles. *Nano Lett.* **2011,** *11*, 701-705.

20. Shemer, G.; Krichevski, O.; Markovich, G.; Molotsky, T.; Lubitz, I.; Kotlyar, A. B. Chirality of Silver Nanoparticles Synthesized on DNA. *J. Am. Chem. Soc.* **2006,** *128*, 11006-11007.

21. Govorov, A. O.; Gun'ko, Y. K.; Slocik, J. M.; Gérard, V. A.; Fan, Z.; Naik, R. R. Chiral nanoparticle assemblies: circular dichroism, plasmonic interactions, and exciton effects. *J. Mater. Chem.* **2011,** *21*, 16806-16818.

22. García-Etxarri, A.; Dionne, J. A. Surface-enhanced circular dichroism spectroscopy mediated by nonchiral nanoantennas. *Phys. Rev. B* **2013,** *87*, 235409.

23. Maoz, B. M.; Chaikin, Y.; Tesler, A. B.; Bar Elli, O.; Fan, Z.; Govorov, A. O.; Markovich, G. Amplification of Chiroptical Activity of Chiral Biomolecules by Surface Plasmons. *Nano Lett.* **2013,** *13*, 1203-1209.

24. Merg, A. D.; Boatz, J. C.; Mandal, A.; Zhao, G.; Mokashi-Punekar, S.; Liu, C.; Wang, X.; Zhang, P.; van der Wel, P. C. A.; Rosi, N. L. Peptide-Directed Assembly of Single-Helical Gold Nanoparticle Superstructures Exhibiting Intense Chiroptical Activity. *J. Am. Chem. Soc.* **2016,** *138*, 13655-13663.

25. Pigliacelli, C.; Sanjeeva, K. B.; Nonappa; Pizzi, A.; Gori, A.; Bombelli, F. B.; Metrangolo, P. In Situ Generation of Chiroptically-Active Gold-Peptide Superstructures Promoted by Iodination. *ACS Nano* **2019,** *13*, 2158-2166.

26. Querejeta-Fernández, A.; Chauve, G.; Methot, M.; Bouchard, J.; Kumacheva, E. Chiral Plasmonic Films Formed by Gold Nanorods and Cellulose Nanocrystals. *J. Am. Chem. Soc.* **2014,** *136*, 4788-4793.

27. Guerrero-Martínez, A.; Auguié, B.; Alonso-Gómez, J. L.; Džolić, Z.; Gómez-Graña, S.; Žinić, M.; Cid, M. M.; Liz-Marzán, L. M. Intense Optical Activity from Three-Dimensional Chiral Ordering of Plasmonic Nanoantennas. *Angew. Chem. Int. Ed.* **2011,** *50*, 5499-5503.

28. Chen, L.; Zheng, J.; Feng, J.; Qian, Q.; Zhou, Y. Reversible modulation of plasmonic chiral signals of achiral gold nanorods using a chiral supramolecular template. *Chem. Commun.* **2019,** *55*, 11378-11381.

29. Funck, T.; Nicoli, F.; Kuzyk, A.; Liedl, T. Sensing Picomolar Concentrations of RNA Using Switchable Plasmonic Chirality. *Angew. Chem. Int. Ed.* **2018,** *57*, 13495-13498.

30. Kuzyk, A.; Schreiber, R.; Fan, Z.; Pardatscher, G.; Roller, E.-M.; Högele, A.; Simmel, F. C.; Govorov, A. O.; Liedl, T. DNA-based self-assembly of chiral plasmonic nanostructures with tailored optical response. *Nature* **2012,** *483*, 311-314.

31. Zhou, C.; Duan, X.; Liu, N. DNA-Nanotechnology-Enabled Chiral Plasmonics: From Static to Dynamic. *Acc. Chem. Res.* **2017,** *50,* 2906-2914.

32. Feng, W.; Kadiyala, U.; Yan, J.; Wang, Y.; DiRita, V. J.; VanEpps, J. S.; Kotov, N. A. Plasmonic nanoparticles assemblies templated by helical bacteria and resulting optical activity. *Chirality* **2020,** *32*, 899-906.

33. Selivanovitch, E.; Douglas, T. Virus capsid assembly across different length scales inspire the development of virus-based biomaterials. *Curr. Opin.Virol.* **2019,** *36*, 38-46.

34. Sasaki, E.; Hilvert, D. Self-Assembly of Proteinaceous Multishell Structures Mediated by a Supercharged Protein. *J. Phys. Chem. B* **2016,** *120*, 6089-6095.

35. Kostiainen, M. A.; Hiekkataipale, P.; Laiho, A.; Lemieux, V.; Seitsonen, J.; Ruokolainen, J.; Ceci, P. Electrostatic assembly of binary nanoparticle superlattices using protein cages. *Nat. Nanotechnol.* **2013,** *8*, 52-6.

36. Fraenkel-Conrat, H. In *Tobacco mosaic virus. The history of tobacco mosaic virus and the evolution of molecular biology*, Plenum: New York, 1986; pp 5-17.

37. Feng, W.; Kim, J.-Y.; Wang, X.; Calcaterra, H. A.; Qu, Z.; Meshi, L.; Kotov, N. A. Assembly of mesoscale helices with near-unity enantiomeric excess and light-matter interactions for chiral semiconductors. *Sci. Adv.* **2017,** *3*, e1601159.

38. Chapman, S. N. in *Plant Virology Protocols: From Viral Sequence to Protein Function, Second Edition.* Humana Press Inc. NJ, U. S. 2008; pp 677.

39. Liljeström, V.; Ora, A.; Hassinen, J.; Rekola, H.; Nonappa; Heilala, M.; Hynninen, V.; Joensuu, J.; Ras, R.; Törmä, P.; Ikkala, O.; Kostiainen, M. Cooperative colloidal self-assembly of metal-protein superlattice wires. *Nat. Commun.* **2017,** *8,* 671.

40. Samal, A.; Sreenivasan, S.; Thalappil, P. Investigation of the role of $NaBH_4$ in the chemical synthesis of gold nanorods. *J. Nanopart. Res.* **2010,** *12*, 1777-1786.

41. Hynninen, V.; Hietala, S.; McKee, J. R.; Murtomäki, L.; Rojas, O. J.; Ikkala, O.; Nonappa. Inverse Thermoreversible Mechanical Stiffening and Birefringence in a Methylcellulose/Cellulose Nanocrystal Hydrogel. *Biomacromolecules* **2018,** *19*, 2795-2804.

42. Mastronarde, D. N. SerialEM: A Program for Automated Tilt Series Acquisition on Tecnai Microscopes Using Prediction of Specimen Position. *Microsc. Microanal.* **2003,** *9*, 1182-1183.

43. Mastronarde, D. N. Automated electron microscope tomography using robust prediction of specimen movements. *J. Struct. Biol.* **2005,** *152*, 36-51.

44. Nonappa, N.; Engelhardt, P. Electron Tomography of Whole Mounts. *Imaging & Microscopy* **2019,** *21*, 22-24.

45. Kremer, J. R.; Mastronarde, D. N.; McIntosh, J. R. Computer Visualization of Three-Dimensional Image Data Using IMOD. *J. Struct. Biol.* **1996,** *116*, 71-76.

46. Engelhardt, P. Three-dimensional reconstruction of chromosomes using electron tomography. *Methods Mol. Biol.* Totowa, NJ, U. S. **2007,** *369*, 365-385.

47. Yang, W. H.; Schatz, G. C.; Van Duyne, R. P. Discrete dipole approximation for calculating extinction and Raman intensities for small particles with arbitrary shapes. *J. Chem. Phys.* **1995,** *103*, 869-875.

48. García de Abajo, F. J. Colloquium: Light scattering by particle and hole arrays. *Rev. Mod. Phys.* **2007,** *79*, 1267-1290.

49. Moroz, A. Depolarization field of spheroidal particles. *J. Opt. Soc. Am. B* **2009,** *26*, 517-527.

50. Bohren, C. F.; Huffman, D. R. *Absorption and Scattering of Light by Small Particles*. John Wiley and Sons: NJ, U.S. 1983; pp 530.

51. Lin, R. D.; Steinmetz, N. F. Tobacco mosaic virus delivery of mitoxantrone for cancer therapy. *Nanoscale* **2018,** *10*, 16307-16313.

52. Anaya-Plaza, E.; Aljarilla, A.; Beaune, G.; Nonappa; Timonen, J. V. I.; de la Escosura, A.; Torres, T.; Kostiainen, M. A. Phthalocyanine–Virus Nanofibers as Heterogeneous Catalysts for Continuous-Flow Photo-Oxidation Processes. *Adv. Mater.* **2019,** *31*, 1902582.

53. Zhang, J.; Zhou, K.; Zhang, Y.; Du, M.; Wang, Q. Precise Self-Assembly of Nanoparticles into Ordered Nanoarchitectures Directed by Tobacco Mosaic Virus Coat Protein. *Adv. Mater.* **2019,** *31*, 1901485.

54. Dujardin, E.; Peet, C.; Stubbs, G.; Culver, J.; Mann, S. Organization of Metallic Nanoparticles Using Tobacco Mosaic Virus Templates. *Nano Lett.* **2003,** *3,* 413-417.

55. Czapar, A. E.; Zheng, Y.-R.; Riddell, I. A.; Shukla, S.; Awuah, S. G.; Lippard, S. J.; Steinmetz, N. F. Tobacco Mosaic Virus Delivery of Phenanthriplatin for Cancer therapy. *ACS Nano* **2016,** *10*, 4119-4126.

56. Sánchez-Iglesias, A.; Grzelczak, M.; Pérez-Juste, J.; Liz-Marzán, L. M. Binary Self-Assembly of Gold Nanowires with Nanospheres and Nanorods. *Angew. Chem. Int. Ed.* **2010,** *49*, 9985-9989.

57. Correa-Duarte, M. A.; Pérez-Juste, J.; Sánchez-Iglesias, A.; Giersig, M.; Liz-Marzán, L. M. Aligning Au Nanorods by Using Carbon Nanotubes as Templates. *Angew. Chem. Int. Ed.* **2005,** *44*, 4375-4378.

58. Li, T.; Zan, X.; Winans, R. E.; Wang, Q.; Lee, B. Biomolecular Assembly of Thermoresponsive Superlattices of the Tobacco Mosaic Virus with Large Tunable Interparticle Distances. *Angew. Chem. Int. Ed.* **2013,** *52*, 6638-6642.

59. Warmke, H. E.; Edwardson, J. R. Electron microscopy of crystalline inclusions of tobacco mosaic virus in leaf tissue. *Virology* **1966,** *30*, 45-57.

60. Niu, Z.; Bruckman, M.; Kotakadi, V. S.; He, J.; Emrick, T.; Russell, T. P.; Yang, L.; Wang, Q. Study and characterization of tobacco mosaic virus head-to-tail assembly assisted by aniline polymerization. *Chem. Commun.* **2006,** 3019-3021.

61. Gibaud, T.; Barry, E.; Zakhary, M. J.; Henglin, M.; Ward, A.; Yang, Y.; Berciu, C.; Oldenbourg, R.; Hagan, M. F.; Nicastro, D.; Meyer, R. B.; Dogic, Z. Reconfigurable self-assembly through chiral control of interfacial tension. *Nature* **2012,** *481*, 348-351.

62. Yeom, J.; Yeom, B.; Chan, H.; Smith, K. W.; Dominguez-Medina, S.; Bahng, J. H.; Zhao, G.; Chang, W. S.; Chang, S. J.; Chuvilin, A.; Melnikau, D.; Rogach, A. L.; Zhang, P.; Link, S.; Král, P.; Kotov, N. A. Chiral templating of self-assembling nanostructures by circularly polarized light. *Nat. Mater.* **2015**, *14*, 66.

63. Nguyen, L.; Dass, M.; Ober, M. F.; Besteiro, L. V.; Wang, Z. M.; Nickel, B.; Govorov, A. O.; Liedl, T.; Heuer-Jungemann, A. Chiral Assembly of Gold–Silver Core–Shell Plasmonic Nanorods on DNA Origami with Strong Optical Activity. *ACS Nano* **2020,** *14*, 7454-7461.

64. Vinegrad, E.; Vestler, D.; Ben-Moshe, A.; Barnea, A. R.; Markovich, G.; Cheshnovsky, O. Circular Dichroism of Single Particles. *ACS Photonics* **2018,** *5*, 2151-2159. 53.

65. Karst, J.; Cho, N. H.; Kim, H.; Lee, H.-E.; Nam, K. T.; Giessen, H.; Hentschel, M. Chiral Scatterometry on Chemically Synthesized Single Plasmonic Nanoparticles. *ACS Nano* **2019,** *13*, 8659-8668.

66. Chaudhari, K.; Pradeep, T. Optical rotation by plasmonic circular dichroism of isolated gold nanorod aggregates. *Appl. Phys. Lett.* **2014,** *105*, 203105/1-203105/4.

67. Kontturi, E.; Laaksonen, P.; Linder, M. B.; Nonappa; Gröschel, A. H.; Rojas, O. J.; Ikkala, O. Advanced Materials through Assembly of Nanocelluloses. *Adv. Mater.* **2018,** *30*, 1703779.

68. Usov, I.; Nyström, G.; Adamcik, J.; Handschin, S.; Schütz, C.; Fall, A.; Bergström, L.; Mezzenga, R. Understanding nanocellulose chirality and structure–properties relationship at the single fibril level. *Nat. Commun.* **2015,** *6*, 7564.

69. Cheng, Z.; Ma, Y.; Yang, L.; Cheng, F.; Huang, Z.; Natan, A.; Li, H.; Chen, Y.; Cao, D.; Huang, Z.; Wang, Y.; Liu, Y.; Yang, R.; Zhu, H. Plasmonic-Enhanced Cholesteric Films: Coassembling Anisotropic Gold Nanorods with Cellulose Nanocrystals. *Adv. Opt. Mater.* **2019,** *7*, 1801816.

70. Majoinen, J.; Hassinen, J.; Haataja, J. S.; Rekola, H. T.; Kontturi, E.; Kostiainen, M. A.; Ras, R. H. A.; Törmä, P.; Ikkala, O. Chiral Plasmonics Using Twisting along Cellulose Nanocrystals as a Template for Gold Nanoparticles. *Adv. Mater.* **2016,** *28*, 5262-5267.

71. Kuzyk, A.; Schreiber, R.; Zhang, H.; Govorov, A. O.; Liedl, T.; Liu, N. Reconfigurable 3D plasmonic metamolecules. *Nat. Mater.* **2014,** *13*, 862-866.

ToC graphic

Spontaneous assembly of cationic gold nanorods along chiral tobacco mosaic virus particles offer a facile route for helical microwires with near-infrared chiral response.